Backscatter in stratified turbulence

Sina Khani[1]

Wind Engineering and Renewable Energy Laboratory (WiRE), École Polytechnique Fédérale de Lausanne (EPFL), Lausanne, Switzerland CH-1015

Department of Applied Mathematics, University of Waterloo, Waterloo, Ontario, Canada N2L 3G1

Michael L. Waite

Department of Applied Mathematics, University of Waterloo, Waterloo, Ontario, Canada N2L 3G1

Abstract

In this paper, kinetic and potential energy transfers around a spectral test filter scale in direct numerical simulations of decaying stratified turbulence are studied in both physical and spectral domains. It is shown that while the domain-averaged effective subgrid scale energy transfer in physical space is a net downscale cascade, it is actually a combination of large values of downscale and upscale transfer, i.e. forward- and backscatter, in which the forward scatter is slightly dominant. Our results suggest that spectral backscatter in stratified turbulence depends on the buoyancy Reynolds number Re_b and the filtering scale Δ_{test}. When the test filter scale Δ_{test} is around the dissipation scale L_d, transfer spectra show spectral backscatter from sub-filter to intermediate scales, as reported elsewhere. However, we find that this spectral backscatter is due to viscous effects at vertical scales around the test filter. It is also shown that there is a non-local energy transfer from scales larger than the buoyancy scale L_b to small scales.The effective turbulent Prandtl number spectra demonstrate that the assumption $Pr_t \approx 1$ is reasonable for the local energy transfer.

Keywords: `Stratified turbulence; Direct numerical simulations; up- and downscale energy transfer`

---

[1]email: sinakhani@uwaterloo.ca

1. Introduction

Large eddy simulations (LES) is an approach for decreasing the computational costs of direct numerical simulations (DNS) of turbulent flows. In LES, the large energy-containing eddies are directly resolved but subgrid scale (SGS) eddies are parametrized. Most SGS parameterizations such as the Smagorinsky [1] and Kraichnan [2] models are based on the Richardson [3] energy-cascade hypothesis, which argued that turbulent kinetic energy is generated at large scales and dissipated at small scales. Richardson's prediction may be valid for the average kinetic energy cascade, but might not be accurate in the local sense. Locally, the energy cascade is the net outcome of forward scatter, i.e. the energy transfer from large to small scales, and the backscatter, which is the reverse energy transfer from small to large scales. For example, Piomelli et al. [4] and Domaradzki et al. [5] have shown that forward- and backscatter are of the same order of magnitude in turbulent channel flow and isotropic decaying turbulence, respectively.

The dynamic SGS scheme, proposed by Germano et al. [6], has been designed to improve the performance of purely dissipative eddy viscosity SGS schemes such as the Smagorinsky [1] model by considering a time- and space-dependent dynamic Smagorinsky coefficient c_s with negative values corresponding to backscatter. However, averaging c_s over a homogeneous direction is often required to avoid numerical instabilities [e.g. 7, 8, 9]. Information about the dynamics of the local energy transfer is therefore lost, and in practice, the averaging procedure removes the local effect of backscatter, because the averaged c_s is usually positive [e.g. 7, 9, 10, 11, 12].

Stratified turbulence is a model for turbulence in the atmospheric mesoscale and oceanic sub-mesoscale, at which fluid motions are strongly affected by stratification but weakly affected by the Earth's rotation [e.g. 13]. The presence of stratification leads to the generation of anisotropic features such as pancake vortices, which in turn lead to the development of different length scales and spec-

2

tral slopes in the horizontal and vertical directions [e.g. 14, 15, 16, 17, 18, 19]. Recently, the dynamics of energy transfer between large and sub-filter scales in stratified turbulence has been studied in wavenumber space [20, 21]. Using DNS of decaying stratified turbulence, Khani & Waite [20] studied the dynamics of horizontal and vertical energy transfer around the Ozmidov scale. It was shown that stratification leads to a non-local energy transfer from large to small horizontal scales when an anisotropic horizontal test cutoff k_c is employed [20]. In addition, the spectral eddy viscosity based on the vertical kinetic energy shows negative values when the flow is subjected to very stable stratification, leading to negative effective turbulent Prandtl number [21].

The performance of different eddy viscosity SGS models (the Smagorinsky, dynamic Smagorinsky and Kraichnan models) has recently been studied in LES of stratified turbulence with isotropic grid resolution [10, 22]. In all cases, it is shown that LES must resolve the buoyancy scale $L_b = 2\pi u_{rms}/N$ to capture the fundamental large scale characteristics of stratified turbulence. Here, u_{rms} and N are the root-mean-square velocity and buoyancy frequency. The resolution criterion for LES of stratified turbulence depends on the SGS model: it requires $\Delta < 0.47L_b$ for the Kraichnan model, $\Delta < 0.24L_b$ for the dynamic Smagorinsky model and $\Delta < 0.17L_b$ for the regular Smagorinsky model [where Δ is the grid spacing, 10, 22]. These criteria are obtained by studying the capability of different SGS models to capture three fundamental features of stratified turbulence: layered structures that break down into Kelvin-Helmholtz (KH) instabilities and small-scale turbulence when shear is large; horizontal wavenumber energy spectra with an approximately $-5/3$ power law at large scales along with a bump (or shallowness) around k_b; and the resolution of regions with small and negative Richardson number, which demonstrate the presence of KH instabilities, overturning and small-scale turbulence. These fundamental features have been reported in several DNS and hyperviscosity simulations of stratified turbulence [e.g. 14, 15, 17, 18, 19, 20, 23, 24, 25, 26]. The importance of L_b implies that LES of stratified turbulence does not require resolution of the smaller Ozmidov scale $L_o = 2\pi(\epsilon/N^3)^{1/2}$, where ϵ is the kinetic energy dissipation rate [10, 22].

As a result, the potential of employing LES with much coarser grids than DNS is promising.

In physical space, backscatter can be calculated from DNS data by filtering velocity fields, and directly measuring the sub-filter scale (SGS) momentum tensor τ_{ij}. Following Piomelli et al. [4], backscatter may be defined by negative values of the effective SGS dissipation rates ϵ_{SGS} and ε_{SGS}, written as

$$\epsilon_{SGS} = -2\tau_{ij}\bar{S}_{ij}, \qquad \varepsilon_{SGS} = -h_j \frac{\partial \bar{\rho}}{\partial x_j}, \tag{1}$$

where $\bar{S}_{ij}$ is the filtered rate of strain. A similar procedure was used recently to analyze SGS backscatter in DNS of reacting turbulence [27], which found that backscatter depends on the dynamics of reacting flows and hence is not just a random and intermittent process. The dynamics of backscatter has not been studied for stratified turbulence. Indeed, the physical mechanisms underlying the dynamics of energy transfer are not completely understood in this context.

In this paper, the dynamics of forward and inverse energy transfer around the Ozmidov scale in DNS of stratified turbulence is studied at different buoyancy Reynolds numbers and using different test filters. In addition, the spectral kinetic and potential energy transfer, and the effective turbulent Prandtl number, are analyzed. The governing equations of motion and formulations for analyzing DNS diagnoses are presented in §2. Section 3 presents the methodology used, and §4 presents the results and discussion. Conclusions are given in §5.

2. Governing equations

The non-dimensional Boussinesq equations are

$$\frac{\partial \boldsymbol{u}}{\partial t} + \boldsymbol{u} \cdot \nabla \boldsymbol{u} = -\nabla p - \frac{1}{Fr_\ell{}^2}\rho\boldsymbol{e}_z + \frac{1}{Re_\ell}\nabla^2\boldsymbol{u}, \tag{2}$$

$$\nabla \cdot \boldsymbol{u} = 0, \tag{3}$$

$$\frac{\partial \rho}{\partial t} + \boldsymbol{u} \cdot \nabla \rho - w = \frac{1}{Re_\ell Pr}\nabla^2\rho, \tag{4}$$

where $\boldsymbol{u} = (u, v, w)$ is the velocity vector, ρ and p are the density and pressure perturbations, respectively; Re_ℓ, Fr_ℓ, and Pr are the initial Reynolds, Froude

4

and Prandtl numbers, respectively, which are defined in terms of the initial velocity and length scales. The density perturbation is nondimensionalized in terms of the constant background density gradient and the initial length scale. We can define the test-filtered variables by applying a filtering operator to the DNS results, e.g. for velocity

$$\bar{\boldsymbol{u}}(\boldsymbol{x}, t) = \int_D G(\hat{\boldsymbol{x}}, \boldsymbol{x}) \boldsymbol{u}(\hat{\boldsymbol{x}}, t) \mathrm{d}\hat{\boldsymbol{x}}, \tag{5}$$

where G is the filtering function and D is the spatial domain. Hence, the governing equations (2-4) can be rewritten for the test-filtered variables as follows

$$\frac{\partial \bar{u}_i}{\partial t} + \frac{\partial}{\partial x_j}(\bar{u}_i \bar{u}_j) = -\frac{\partial \bar{p}}{\partial x_j} - \frac{1}{Fr_\ell^2}\bar{\rho}\boldsymbol{e}_z + \frac{1}{Re_\ell}\frac{\partial^2 \bar{u}_i}{\partial x_j \partial x_j} - \frac{\partial \tau_{ij}}{\partial x_j}, \tag{6}$$

$$\frac{\partial \bar{u}_i}{\partial x_i} = 0, \tag{7}$$

$$\frac{\partial \bar{\rho}}{\partial t} + \frac{\partial}{\partial x_j}(\bar{\rho}\bar{u}_j) - \bar{w} = \frac{1}{Re_\ell Pr}\frac{\partial \bar{\rho}}{\partial x_j \partial x_j} - \frac{\partial h_j}{\partial x_j}, \tag{8}$$

where

$$\tau_{ij} = \overline{u_i u_j} - \bar{u}_i \bar{u}_j, \qquad h_j = \overline{\rho u_j} - \bar{\rho}\bar{u}_j, \tag{9}$$

are the SGS momentum and density fluxes which are known since DNS resolves both the test-filtered and sub-test-filter scales. Using the measured SGS momentum flux τ_{ij}, we can calculate the SGS dissipation field ϵ_{SGS} through equation (1), which gives the local rate of energy transfer between the test-filtered scales and the sub-test-filter motions. Following Piomelli et al. [4], if ϵ_{SGS} is positive, then the kinetic energy transfers from the test-resolved to the SGS motions (forward scatter); however, if ϵ_{SGS} is negative, kinetic energy is transferred in the opposite direction (backscatter), i.e. $\epsilon_{SGS} = \epsilon^+ + \epsilon^-$, where

$$\epsilon^\pm = \frac{1}{2}(\epsilon_{SGS} \pm |\epsilon_{SGS}|). \tag{10}$$

Similarly, forward- and backscatter of potential energy is

$$\varepsilon^\pm = \frac{1}{2}(\varepsilon_{SGS} \pm |\varepsilon_{SGS}|). \tag{11}$$

85   In the wavenumber domain, assuming periodic boundary conditions and a sharp spectral filter with wavenumber k_c, we can use the measured SGS fluxes in

5

(9) to calculate the kinetic and potential effective SGS energy transfer following Pope [9] as

$$T_k(k|k_c, t) = \frac{1}{2} \langle F_j \hat{\tilde{u}}_j^* + F_j^* \hat{\tilde{u}}_j \rangle_k, \tag{12}$$

$$T_p(k|k_c, t) = \frac{1}{2} \langle J \hat{\tilde{\rho}}^* + J^* \hat{\tilde{\rho}} \rangle_k, \tag{13}$$

where F_j and J are the Fourier coefficients of the SGS fluxes $\partial \tau_{ij}/\partial x_j$ and $\partial h_j/\partial x_j$, respectively, where $*$ is complex conjugate and the angle bracket $\langle \cdots \rangle_k$ denotes summing of the Fourier modes over spherical shells of constant radius k. Here, $k = |\boldsymbol{k}|$ and $\boldsymbol{k} = (k_x, k_y, k_z)$ is the three dimensional wavevector. The $|k_c$ notation in (12-13) underlines that the transfers are computed relative to a particular filter wavenumber [9]. The physical and spectral SGS energy transfer are related: the sum of the SGS transfer spectra equals the domain-averaged SGS dissipation rate, written as

$$\sum_k T_k(k|k_c, t) = \epsilon_{SGS}(k_c, t), \tag{14}$$

$$\sum_k T_p(k|k_c, t) = \varepsilon_{SGS}(k_c, t), \tag{15}$$

where the sum is over all wavenumbers resolved by the filter. However, there is not a straightforward connection between the spectral and physical backscatter (i.e. negative values of T_k, T_p, ϵ_{SGS} and ε_{SGS}) since they result from different, physical vs. wavenumber, perspectives. Nevertheless, the wavenumbers associated with negative transfers, i.e. spectral backscatter, likely give some indication of the length scales associated with ϵ^-.

In addition, the effective eddy viscosity $\nu_e(k|k_c, t)$ and the effective eddy diffusivity $D_e(k|k_c, t)$ are defined as

$$\nu_e(k|k_c, t) = \frac{T_k(k|k_c, t)}{2k^2 E(k, t)}, \qquad D_e(k|k_c, t) = \frac{T_p(k|k_c, t)}{2k^2 E_p(k, t)}, \tag{16}$$

where $E(k, t)$ and $E_p(k, t)$ are the kinetic and potential energy spectra. Using these, the effective turbulent Prandtl number can be written as

$$Pr_t(k|k_c, t) = \frac{\nu_e(k|k_c, t)}{D_e(k|k_c, t)}. \tag{17}$$

6

Stratified turbulence is characterised by large Reynolds number $Re = u_{rms}l_h/\nu$ and small horizontal Froude number $Fr_h = u_{rms}/Nl_h$ such that the buoyancy Reynolds number $Re_b = ReFr_h^2$ is also large [e.g. 17]. Here, l_h and ν are the horizontal length scale and molecular viscosity, respectively. The dissipation length scale is given by $k_d = (\epsilon/\nu^3)^{1/4}$. For decaying turbulence, the maximum k_d and Re_b happen at the time when ϵ is maximum.

3. Methodology

An idealized case study for decaying stratified turbulence is designed in a cubic domain with triply periodic boundary conditions with side length $L = 2\pi$. Taylor-Green (TG) vortices of size π are used as initial conditions, i.e.

$$\boldsymbol{u}(\boldsymbol{x}, 0) = \cos(z)[\cos(x)\sin(y), -\sin(x)\cos(y), 0]. \tag{18}$$

Also, approximately 10% of the initial energy in the form of low-level noise perturbs the initial TG vortices isotropically. Noise is restricted to small wavenumbers $k < 10$. The domain is smaller than that used in Khani & Waite [20] to allow for higher effective spatial resolution, which leads to a decrease in computation time [as in e.g. 5]. The spectral transform method is employed for computing spatial derivatives, along with the two-thirds rule to eliminate aliasing errors from x, y and z directions. The number of grid points is given by n, and so the effective grid spacing is $\Delta = 1.5L/n$ and the maximum wavenumber is $k_{max} = n/3$ in both horizontal and vertical directions. Resolutions are chosen to resolve the Kolmogorov dissipation wavenumber k_d, with $k_{max}/k_d > 0.7$ in all cases. The explicit third-order Adams-Bashforth scheme is used for time-stepping of all terms except the diffusion terms, for which the implicit trapezoidal method is employed.

Simulations with six different initial Reynolds number $Re_\ell = 1350, 3030, 6400, 10900, 14700$ and 18000, and a range of the initial Froude number Fr_ℓ from 0.12 to ∞ are considered. These parameters yield layer thickness, which are given by the buoyancy scale [e.g. 19, 20], that are several times smaller than

the domain height (i.e. buoyancy wavenumber $k_b = 2\pi/L_b > 1$). Four different sharp spectral test cutoff filters $k_c = 20$, 40, 80 and 160 are employed to study the spectral energy transfer between scale. The horizontal length scale l_h is calculated using the Taylor hypothesis, u_{rms} is set to $\sqrt{E(t)}$ because the vertical kinetic energy is relatively small, and $Pr = 1$. The simulations proceed similarly to other studies of TG stratified turbulence [e.g. 20, 23, 25]: the initial vortices evolve into thin pancake vortices which ultimately, for $Re_b \gtrsim 1$, develop KH instabilities and patches of small-scale turbulence. Table 1 gives the parameters and identifiers for each simulation, including Re_ℓ, Fr_ℓ and n; range of turbulent buoyancy Reynolds and horizontal Froude numbers from when ϵ is maximum up to the end of simulation; ratio k_{max}/k_d where $k_d = 2\pi/L_d$; buoyancy and Ozmidov wavenumbers k_b and k_o, where $k_o = 2\pi/L_o$; the time interval Δt_{avg} over which energy and transfer spectra are averaged; and the time at which the total viscous dissipation rate ϵ_{tot} is maximum.

4. Results & discussion

4.1. Overview of simulations

Figure 1 shows time series of the total energy and dissipation rates, in the top and bottom panels, respectively, where the left panels correspond to cases with $Re_b \gtrsim 1$ and the right panels show those with $Re_b \lesssim 1$. For the unstratified case, a quick drop in the total energy level and a maximum in the total dissipation rate are visible at $t \approx 9$. Increased stratification or decreased Reynolds number postpones the time of the energy decrease and maximum dissipation. For example, the case with $Re_\ell = 10900$ and $Fr_\ell = 0.16$ has only a small decrease in energy up to $t \approx 20$, while the maximum dissipation rate occurs around $t = 22$ (figures 1a,c). These trends suggest that by increasing stratification or decreasing the Reynolds number, i.e. by decreasing the buoyancy Reynolds number, the occurrence of turbulence is postponed [in line with 20, 23]. Interestingly, the

8

Table 1: List of numerical simulations and parameters

| Identifier	Re_ℓ	Fr_ℓ	n	Re_b	Fr_h	k_{max}/k_d	k_b	k_o	Δt_{avg}	t of ϵ_{tot}^{max}
R147F0.6	14700	0.64	960	$8.60 - 21.30$	$0.024 - 0.033$	$1.0 - 1.2$	$5.1 - 9.4$	$33.0 - 52.1$	$10 \le t \le 14$	11.5
R180F0.5	18000	0.48	960	$7.10 - 14.34$	$0.023 - 0.027$	$0.8 - 1.0$	$7.8 - 12.0$	$51.3 - 73.1$	$16 \le t \le 20$	18.5
R109F0.1	10900	0.16	768	$0.81 - 1.45$	0.009	$0.9 - 1.0$	$20.8 - 28.1$	$217.4 - 290.6$	$20 \le t \le 24$	21.5
R64F0.6	6400	0.64	384	$4.15 - 10.13$	$0.028 - 0.034$	$0.7 - 0.9$	$5.5 - 9.1$	$31.5 - 49.2$	$13 \le t \le 17$	14.1
R30F0.5	3030	0.48	512	$1.30 - 2.47$	$0.023 - 0.035$	$1.7 - 2.0$	$7.8 - 12.5$	$50.7 - 69.8$	$15 \le t \le 19$	17.6
R30F0.2	3030	0.24	512	$0.33 - 1.00$	$0.015 - 0.021$	$1.5 - 2.0$	$15.9 - 24.2$	$113.0 - 197.5$	$18 \le t \le 22$	20.2
R30F0.1	3030	0.12	512	$0.12 - 0.19$	0.007	$1.6 - 1.8$	$29.5 - 37.6$	$367.0 - 468.5$	$25 \le t \le 29$	27.4
R13F0.5	1350	0.5	256	$0.70 - 1.13$	$0.033 - 0.041$	$1.5 - 1.7$	$9.0 - 12.8$	$50.0 - 63.5$	$20 \le t \le 24$	22.5
R30	3030	∞	512			$1.2 - 2.1$			$7 \le t \le 11$	8.8
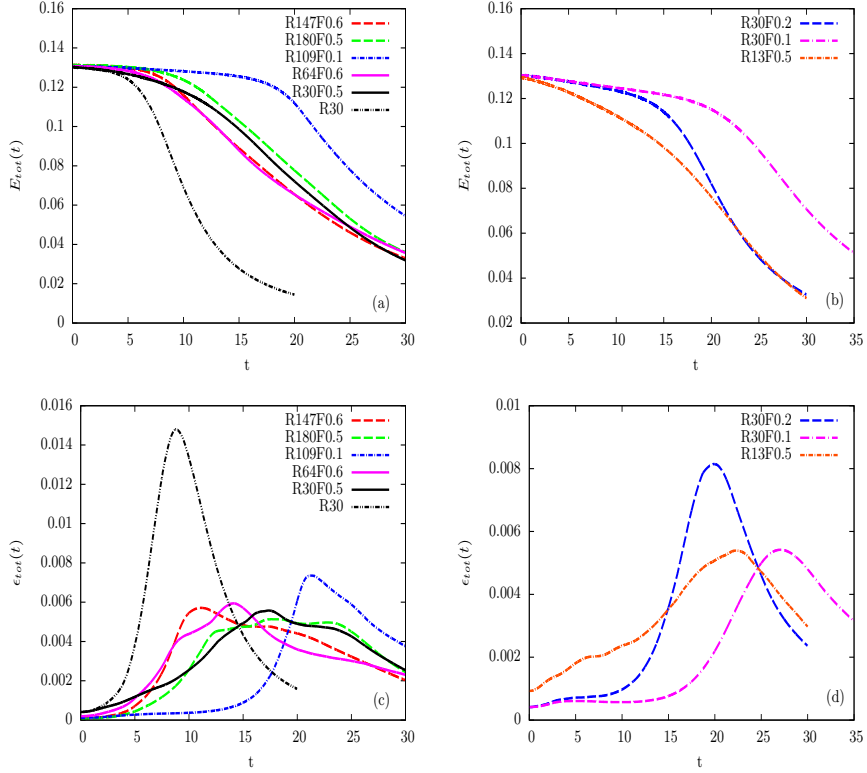
Figure 1: Time series of (a,b) total energy and (c,d) total dissipation rate. The left panels correspond to cases with $Re_b \gtrsim 1$ and the right panels show those with $Re_b \lesssim 1$ (see table 1 for the identifiers).

three cases with the highest Re_b show very similar total energy and dissipation rate (i.e. solid green, solid magenta and dashed red lines in figures 1a,c). In addition, the simulation with $Re_\ell = 3030$ and $Fr_\ell = 0.48$ has similar energy and dissipation time series to the case with the same initial Froude number and $Re_\ell = 18000$ (solid black and dashed green curves in figures 1a,c).

Figure 2(a,b) shows the normal horizontal component of the vorticity ω_y on the x-z plane for the high resolution case with $Re_\ell = 14700$ and $Fr_\ell = 0.64$ at $t = 15$, and the case with $Re_\ell = 10900$ and $Fr_\ell = 0.16$ at $t = 20$, which are around the time of maximum viscous dissipation. At strong stratification, $\omega_y \approx \partial u / \partial z$, so these figures show the x component of the vertical shear. Lay-

10

erwise structures along with KH instabilities are visible in both cases. In addition, small-scale features are present, which seem to correspond to the breakdown of KH billows into smaller-scale turbulence (the case with larger Re_b has more regions with instabilities and turbulence as seen in figures 2a,b). The time-averaged probability distribution of the local Richardson number Ri over $10 \leq t \leq 14$ for the high resolution case with $Fr_\ell = 0.64$, and over $20 \leq t \leq 24$ for the simulation with $Re_\ell = 10900$ and $Fr_\ell = 0.16$ are shown in figure 2(c). The histograms are peaked around 0 and present a long tail for $Ri > 0$ and a rapid drop off for negative Ri. The points with small and negative local Richardson number suggest generation of KH instabilities and overturning, respectively (in line with figures 2a,b). It is shown that increased Re_b leads to generation of more points with small and negative Ri (figure 2). For smaller Re_b, regions of KH instabilities and overturning are reduced or suppressed entirely [not shown; see 30]. Similar behaviours are seen in LES of stratified turbulence in which increased resolution or decreased stratification leads to more resolved KH instabilities and overturning [10, 22].

The time-averaged kinetic energy and dissipation spectra are shown in figure 3 (similar to figure 1, left panels correspond to cases with $Re_b \gtrsim 1$ and right panels shows those with $Re_b \lesssim 1$). The time averaging is performed over a time interval that is approximately centered around the time of maximum $\epsilon_{tot}(t)$ (as shown in table 1). Similar to previous studies [e.g. 20, 23, 28, 29], increased stratification or decreased Reynolds number steepens the slope of the spectra (figure 3). The spectral slopes for all simulations over the range $10 \leq k \leq 70$ are given in table 2. We use the least-squares method to measure these slopes. Overall, decreasing the buoyancy Reynolds number Re_b suppresses the onset of turbulence and steepens the spectral power law (see table 2). Arrows in figure 3 indicate locations of the test cutoffs $k_c = 20$, 40, 80 and 160 (the latter two only for the larger Re_b cases), which are used in the next sections for measuring the energy transfer between scales.
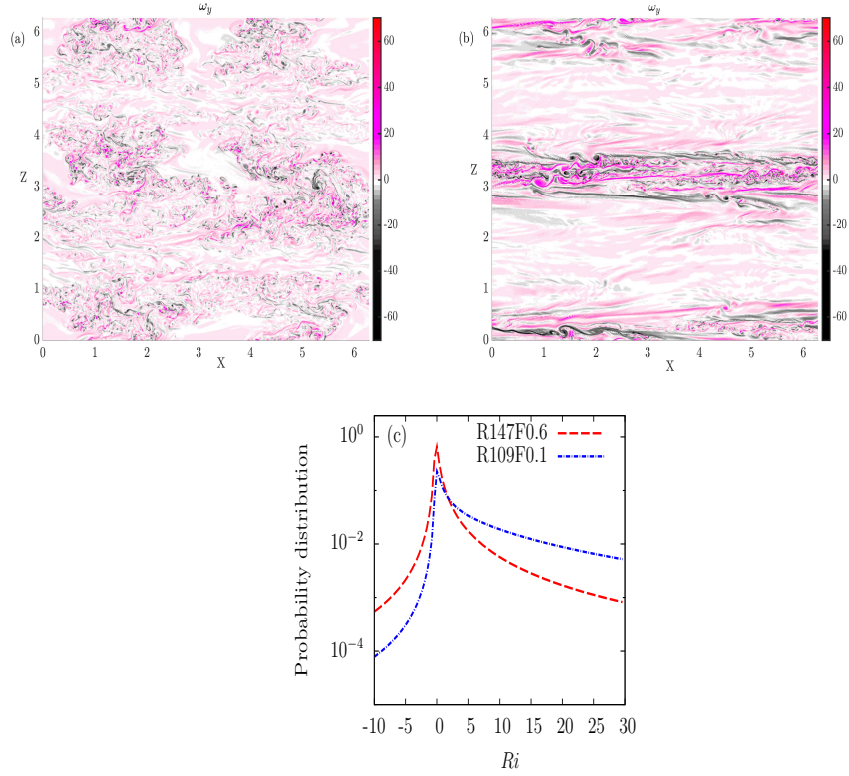
11

Figure 2: The horizontal component of vorticity field ω_y on the x-z plane at $y \approx 0.25$ (a) for the high resolution case with $Re_\ell = 14700$ and $Fr_\ell = 0.64$ at $t = 15$, and (b) for the case with $Re_\ell = 10900$ and $Fr_\ell = 0.16$ at $t = 20$. (c) Averaged probability distribution of the local Richardson number Ri over $10 \le t \le 14$ for the case in (a) and over $20 \le t \le 24$ for the case in (b) – only the segment $-10 \le Ri \le 30$ is shown. Histograms are normalized by bin size to get the probability distribution: 100 bins over $-10 \le Ri \le 30$ ($\Delta Ri = 0.4$).
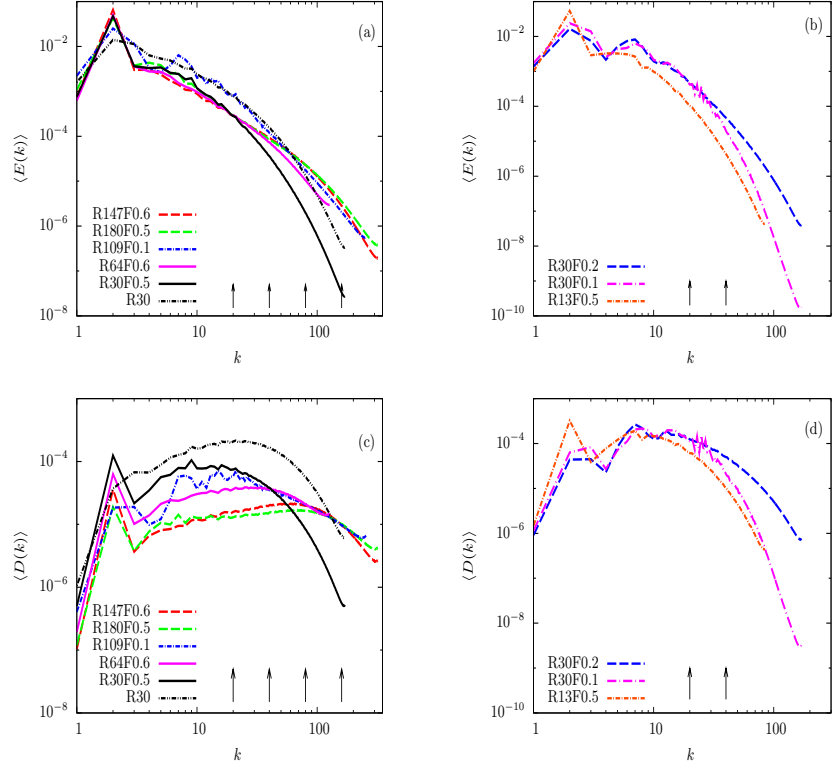
Figure 3: (a,b) Time-averaged kinetic energy spectra and (c,d) time-averaged dissipation spectra $D(k) = 2\nu k^2 E(k)$. The left panels correspond to cases with $Re_b \gtrsim 1$ and right panels show those with $Re_b \lesssim 1$. Arrows indicate the location of the test cutoff $k_c = 20$, 40, 80 and 160.

13

Table 2: Spectral slopes over $10 \leq k \leq 70$.

Identifier	Spectral slope
R147F0.6	-1.7
R180F0.5	-1.8
R109F0.1	-2.5
R64F0.6	-2.1
R30F0.5	-3.1
R30F0.2	-3.3
R30F0.1	-4.7
R13F0.5	-4.8
R30	-2.5

4.2. Energy transfer in physical space

The forward- and backscatter components of the effective SGS kinetic and potential dissipation rates ϵ_{SGS} and ε_{SGS} for $k_c = 40$ are shown in figure 4 (left panels for cases with $Re_b \gtrsim 1$ and right panels for those with $Re_b \lesssim 1$). The maximum forward- and backscatter happens around the time when the total kinetic plus potential energy dissipation rate ϵ_{tot} is peaked (see figures 1c,d). Increased stratification or decreased Reynolds number decreases the amount of forward- and backscatter, and also postpones the peaks. As a result, decreased Re_b reduces forward- and backscatter, and weakens their peak values (figure 4). These results demonstrate that the presence of stratification decreases energy transfer between large and sub-filter scales, i.e. both up- and downscale energy transfers are reduced by increasing stratification [28, 29]. As seen above for the viscous dissipation rates, the three simulations with largest Re_b have similar $\epsilon^{\pm}$ and $\varepsilon^{\pm}$ time series, which peak at an earlier time than all the other stratified cases.

Figure 5 shows the net kinetic and potential effective SGS energy transfers (i.e. ϵ_{SGS} and ε_{SGS}) with $k_c = 40$. Since the net transfer values are positive, this figure demonstrates that the effective SGS energy transfer is downscale,
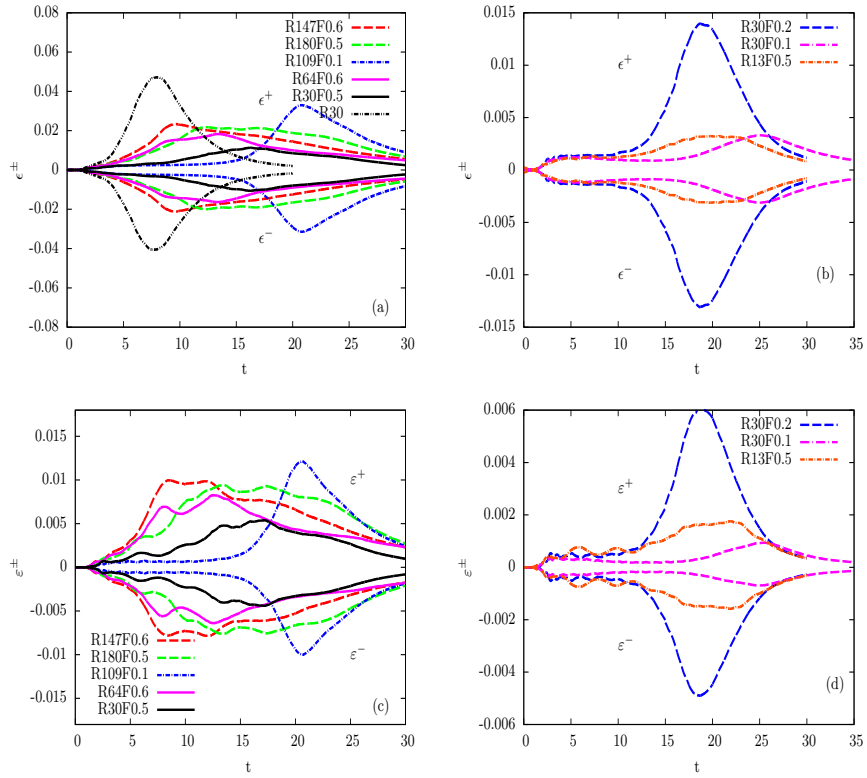
14

Figure 4: Time series of forward- and backscatter components of the domain-averaged effective SGS dissipation rate at $k_c = 40$: (a,b) kinetic and (c,d) potential. The left panels correspond to cases with $Re_b \gtrsim 1$ and the right panels show those with $Re_b \lesssim 1$.

15

and ϵ_{SGS} and ε_{SGS} are peaked around the time that the total viscous dissipa-
tion rate ϵ_{tot} is peaked. It is interesting that the effective SGS energy transfer
results from the superposition of significant forward- and backscatter, the sum
of which is smaller than the individual $\epsilon^{\pm}$ and $\varepsilon^{\pm}$ by almost one order of mag-
nitude (figure 4 compared to figure 5). Similar findings have been reported for
unstratified turbulence [e.g. 4] and reacting turbulence [27]. In addition, our
results show that the domain fraction for backscatter is very close to forward
scatter (around 50% for each) for the high resolution case with $Re_\ell = 14700$ and
$Fr_\ell = 0.64$. This trend suggests that the local volume fraction of backscatter is
as important as forward scatter for stratified turbulence in the physical domain
[in line with results for isotropic turbulence, e.g. 4]. Also, increased Reynolds
number or decreased stratification leads to an increase on the ratios of $\epsilon_{SGS}/\epsilon^{+}$
and $\epsilon_{SGS}/\epsilon^{-}$ (not shown).

4.2.1. Effects of changing the test cutoff k_c

Figure 6 shows the effects of using different test cutoffs on the up- and down-
scale energy transfer when $Re_b \gtrsim 1$. Results from a smaller cutoff wavenumber
$k_c = 20$ (black) are compared to results for the larger cutoff $k_c = 40$ (grey). We
consider these two test filters because they are around or smaller than k_o for
the stratified cases (see table 1). For early times, the forward- and backscatter
are slightly larger for $k_c = 20$ compared to those for $k_c = 40$. However, as
time evolves towards the maximum dissipation, the up- and downscale trans-
fers get slightly larger for the larger cutoff wavenumber $k_c = 40$. Overall, the
effects on these time series of changing the test cutoff k_c are very minor. These
trends might be a sign of self similarity of energy transfer towards small scales
for the averaged-domain SGS dissipation. Similar trends in which forward- and
backscatter in physical space are almost independent to the filter width are re-
ported for unstratified turbulence [4]. In conclusion, these results suggest that
the averaged-domain SGS dissipation is almost independent of the ratio k_c/k_b
or k_c/k_o. In the next section, we investigate the dependence on these ratios in
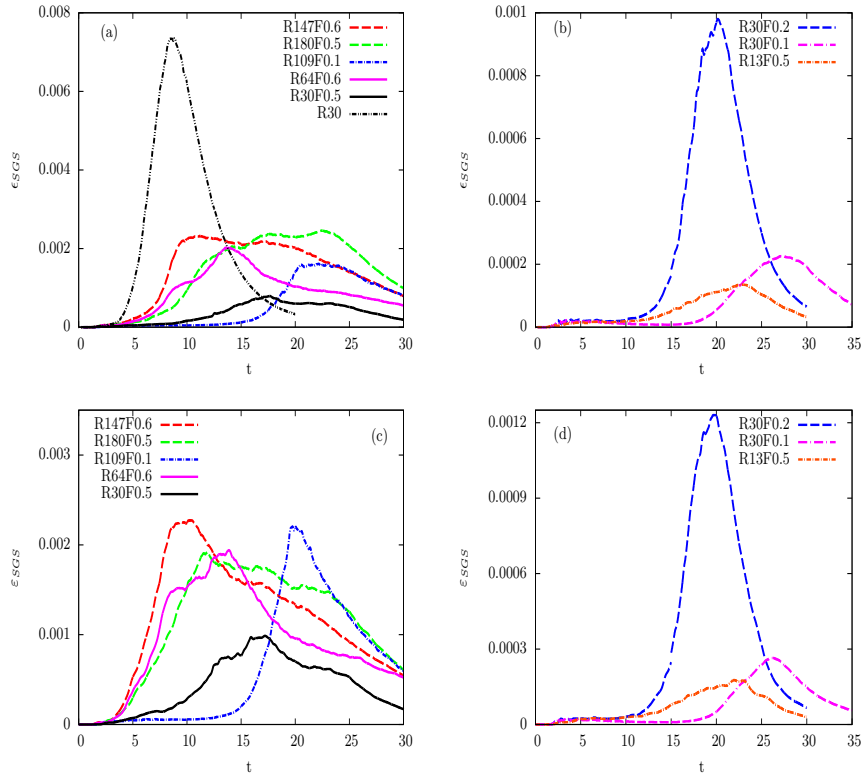wavenumber space, where more differences become apparent.

16

Figure 5: Time series of the domain-averaged effective SGS dissipation rate at $k_c = 40$: (a,b) kinetic and (c,d) potential. The left panels correspond to cases with $Re_b \gtrsim 1$ and the right panels show those with $Re_b \lesssim 1$.
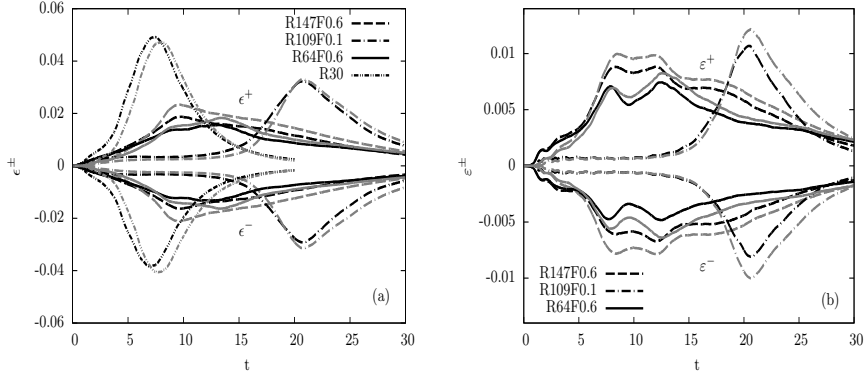
Figure 6: Time series of forward- and backscatter components of the domain-averaged effective SGS dissipation rate for $k_c = 20$ (black colour) and $k_c = 40$ (grey colour): (a) kinetic and (b) potential.

4.3. Energy transfer in wavenumber space

The averaged effective SGS kinetic and potential energy transfer spectra for
$k_c = 40$ are shown in figure 7 (left panels correspond to cases with $Re_b \gtrsim 1$
and right panels show $Re_b \lesssim 1$). According to our definitions in equations
(12-13), positive values of $\langle T_k(k|k_c,t) \rangle$ and $\langle T_p(k|k_c,t) \rangle$ correspond to down-
scale energy transfer from above to below the filter scale, and negative values
denote backscatter. For the unstratified simulation and stratified cases with
$Re_\ell = 18000$ and $Fr_\ell = 0.48$, $Re_\ell = 10900$ and $Fr_\ell = 0.16$, and $Re_\ell = 6400$,
14700 and $Fr_\ell = 0.64$, which are cases with the largest Re_b, no backscatter
is observed at any wavenumber. However, increased stratification along with
decreased Reynolds number results in the upscale transfer of kinetic energy
over intermediate scales $0.1 \lesssim k/k_c \lesssim 0.7$ (figures 7a,b). These trends sug-
gest that by reducing Re_b to be around 1 or smaller (i.e. reducing the spectral
gap between buoyancy and Ozmidov wavenumbers to the viscous dissipation
wavenumber k_d), backscatter emerges in stratified turbulence over an interme-
diate range of wavenumbers (recall, however, that the net SGS transfer, i.e. the
sum of these transfer spectra, is still downscale; see figure 5). All simulations
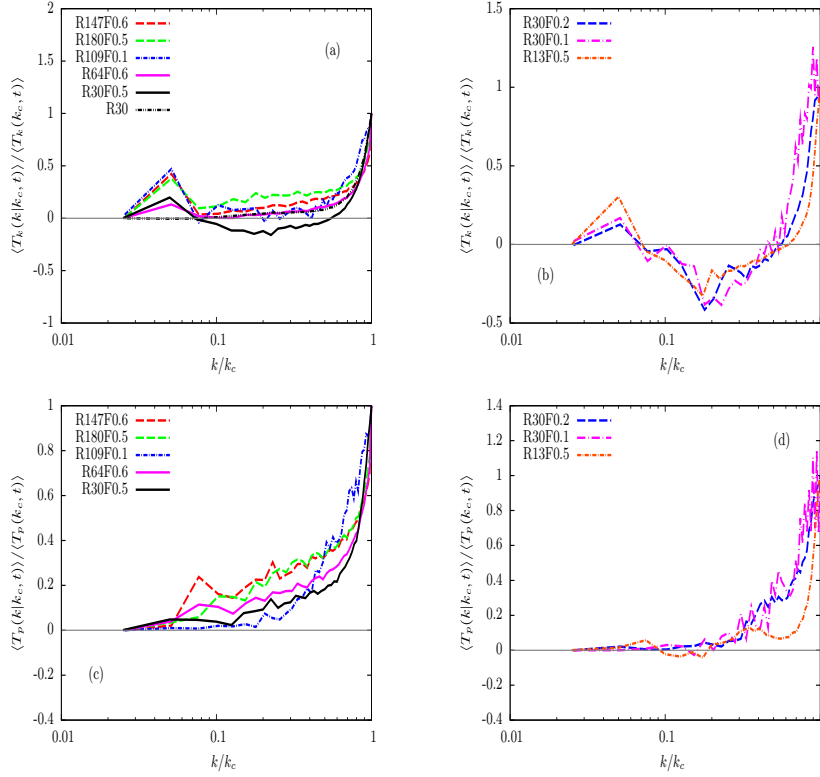with Re_b similar to or less than 1 (i.e. $Re_b \leq 1.45$) exhibit backscatter emerges

18

Figure 7: Averaged effective SGS (a,b) kinetic and (c,d) potential energy transfer spectra for $k_c = 40$. The left panels correspond to cases with $Re_b \gtrsim 1$ and the right panels show those with $Re_b \lesssim 1$. The solid grey line indicates zero.

over intermediate wavenumbers. For the case with $Re_\ell = 10900$ and $Fr_\ell = 0.16$, backscatter occurs at a few discrete wavenumbers; for all other cases, it occurs for a broad range of intermediate wavenumbers. Spectral backscatter is not seen in the effective SGS potential energy transfer spectra for any parameter values (figures 7c,d).

The averaged horizontal and vertical wavenumber effective SGS kinetic and potential energy transfer spectra for the cases with $Re_\ell = 3030$ and $Fr_\ell = 0.24$, and $Re_\ell = 18000$ and $Fr_\ell = 0.48$ are shown in figure 8. It is clear that the case with $Re_b \approx 14$ does not show any spectral backscatter in total, horizontal, or vertical wavenumbers (figure 8c,d). However, the case with $Re_\ell = 3030$ and

19

$Fr_\ell = 0.24$ ($Re_b \approx 1$) shows backscatter at large horizontal and small vertical scales (figure 8a). The sign of the SGS transfer into $k_h = 0$ is the same as the sign of the transfer into small but non-zero k_h (not shown). To further examine this backscatter, and in particular its dependence on Reynolds number, we have performed a series of simulations in which the initial Reynolds number is systematically increased at fixed initial Froude number, thereby increasing the buoyancy Reynolds number. In particular, we consider cases with $Fr_\ell \approx 0.1$ and $Re_\ell = 3030, 10900$, and $Fr_\ell = 0.48$ and $Re_\ell = 3030, 18000$. Interestingly, increased Re_ℓ (and hence Re_b) leads to decreasing, and finally an elimination, of the backscatter (see dot-dashed cyan and blue lines, and black solid and dashed green lines in figures 7a,b). Increased Re_ℓ leads to a decrease in the Kolmogorov scale L_d and an increase in the ratio Δ_{test}/L_d (see below).

By contrast, the horizontal and vertical effective SGS potential energy transfer spectra do not show backscatter (figure 8b). The lack of backscatter in potential energy could be due to the large-scale flow induced by the initial TG vortices, which have no potential energy [similar results were found in e.g. 21]. Also, it is worthwhile mentioning that the existence of spectral backscatter is not an artifact of the domain size. We have run a new simulation with $Re_\ell = 3030$ and $Fr_\ell = 0.24$, and $L = 4\pi$, while Δ is approximately fixed, to evaluate the effects of domain size on the spectral backscatter. The resulting transfer spectrum is similar to that shown in figure 8a (plots are not shown).

4.3.1. Effects of changing the test cutoff k_c

By decreasing the location of the test cutoff wavenumber k_c from 40 to 20, spectral SGS kinetic and potential energy transfers change dramatically (figures 9). The magnitudes of effective SGS energy transfers are increased using smaller k_c. In addition, the spectral kinetic energy transfer show less backscatter than was observed with $k_c = 40$. Indeed, in some cases that showed backscatter with $k_c = 40$, the backscatter is completely eliminated with $k_c = 20$. As a result, by moving the test cutoff k_c towards small wavenumbers, the upscale energy transfer is reduced or eliminated. For example, the stratified case with $Re_\ell =$
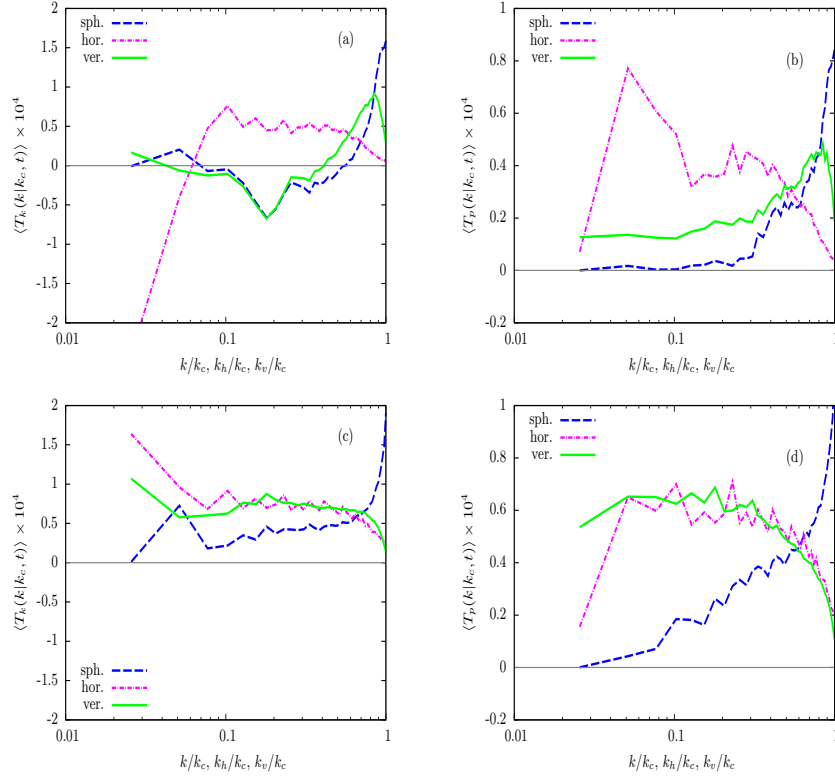
20

Figure 8: Averaged horizontal and vertical wavenumber effective SGS (a,c) kinetic and (b,d) potential energy transfer spectra for cases with (a,b) $Re_\ell = 3030$ and $Fr_\ell = 0.24$, and (c,d) $Re_\ell = 18000$ and $Fr_\ell = 0.48$, when $k_c = 40$. Spectra are shown as functions of total, horizontal and vertical wavenumbers. The k spectra (blue dashed lines in figure 8) show those corresponding curves that were shown in figure 7.
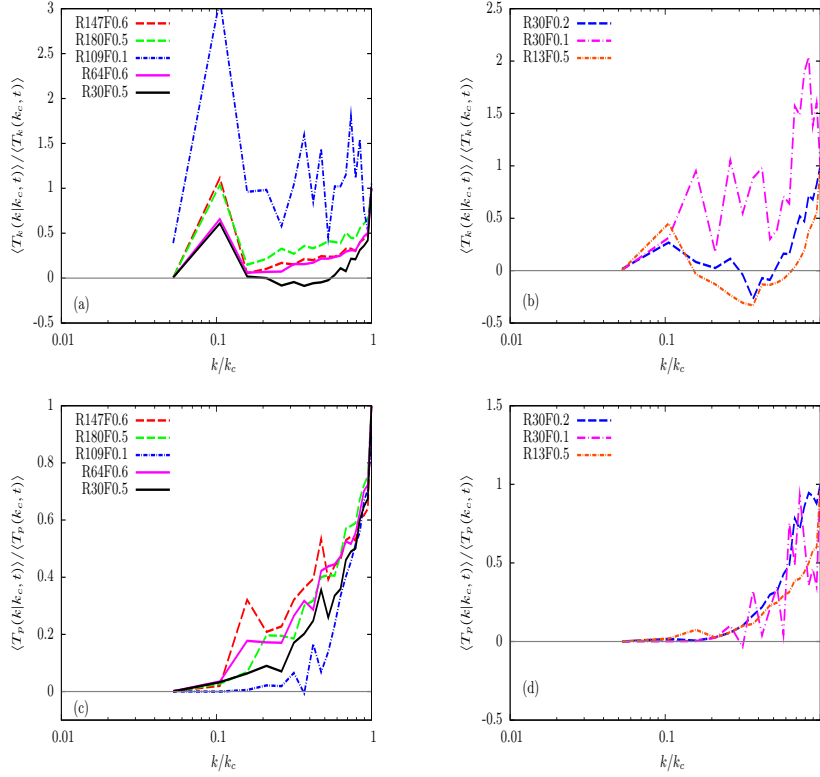
21

Figure 9: Averaged effective SGS (a,b) kinetic and (c,d) potential energy transfer spectra for $k_c = 20$. The left panels correspond to cases with $Re_b \gtrsim 1$ and the right panels show those with $Re_b \lesssim 1$. The solid grey line indicates zero.

3030 and $Fr_\ell = 0.12$ shows no backscatter when $k_c = 20$ (figure 9b), in contrast with the corresponding results when $k_c = 40$ (figure 7b). In fact, in almost all of the simulations that showed spectral backscatter with $k_c = 40$ in figure 7, backscatter is eliminated or occurs over a narrow range of wavenumbers when $k_c = 20$ as seen in figure 9. These trends suggest that the upscale energy transfer happens from sub-test-filter scales, which are affected by viscous layering for small Re_b, towards the smaller test-resolved scales (see figures 7 and 9).

To investigate the dependence of backscatter on k_c, we consider the relationship between k_c and the viscous scales in stratified turbulence. The viscous scale is traditionally measured by the Kolmogorov scales L_d; additionally, in

22

stratified turbulence at low $Re_b \lesssim 1$, stratified turbulence has a viscously layered structure, with vertical layer thickness of $L_{visc} = l_h/\sqrt{Re}$, at which viscous effects are important [e.g. 17]. In our simulations with $Fr_\ell \approx 0.1$, $L_{visc} \approx 0.04$ and 0.08 when $Re_\ell = 10900$ and 3030, respectively. As a result, the test filter scales are clearly affected by viscosity at smaller Re, less so at larger Re. If we compare L_{visc} with the test-filter width $\Delta_{test} = \pi/k_c$, which is around 0.08 for $k_c = 40$, it is clear that with increasing Re, L_{visc} decreases in comparison with Δ_{test}, which could account for the elimination of backscatter.

In a similar examination at higher Re_b, we calculate the averaged effective SGS kinetic energy transfer spectra for the high resolution case with $Fr_\ell = 0.64$ when k_c moves from 20 to 160 (figure 10). It is clear that by increasing the value of k_c from 20 towards the viscous dissipation range (i.e. 160, see the arrows in figure 3a), negative kinetic energy transfer spectra emerges in the intermediate range (figure 10). Consistent with our results in figures 7 and 9, if we move Δ_{test} from $\gg L_d$ to $\lesssim L_d$, backscatter occurs even at large Re_b.

Figure 11 summarizes the presence or not of spectral backscatter by systematical plots of the ratios of the test filter scale to the key scales of stratified turbulence: the buoyancy, Ozmidov, viscous and Kolmogorov scales, versus the buoyancy Reynolds number Re_b for all simulations when k_c varies from 20 to 160. Symbols indicate whether spectral backscatter is observed or not. It is clear from the above that at fixed Re_b, increased Δ_{test} leads to a decrease in spectral backscatter and finally elimination of the spectral upscale transfer (see figures 7, 9). At fixed k_c and Fr_h, the spectral backscatter decreases and finally disappears with increased Re (figures 7, 9). Also, at fixed Re_b, if we increase k_c towards the dissipation range, the spectral energy transfer plateau decreases and even become negative when k_c is very close to k_d (figures 10 and 11a). Figure 11 shows that, at least for $Re_b \gtrsim 10$, there is a clear threshold separating cases with and without spectral backscatter when the ratio Δ_{test}/L_d is considered. For $Re_b \gtrsim 10$, backscatter occurs when $\Delta_{test}/L_d < 1.2$ and is eliminated when this ratio is > 1.2 (figure 11a). In this regime, backscatter depends on both Re_ℓ and Fr_ℓ insofar as they determine Re_b. Beyond that, it
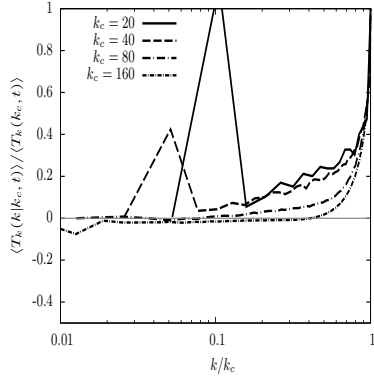
23

Figure 10: Averaged effective SGS kinetic energy transfer spectra for the high resolution case with $Re_\ell = 14700$ and $Fr_\ell = 0.64$ when different test cutoff filters k_c are applied. The solid grey line indicates zero.

is mainly Re_ℓ that matters, as it determines L_d. The behaviour for $Re_b \lesssim 1$ is more complicated, but the trend discussed above – backscatter appears for sufficiently small Δ_{test} – is clear. The lack of a clear threshold on Δ_{test}/L_d at small Re_b may be due to the fact that these simulations are on the edge of the stratified turbulence regime.

We speculate that there may be a similar relation between the viscous scale and test-filter width in DNS of Remmler & Hickel [21], who have also reported spectral backscatter in DNS of stratified turbulence. Using $l_h = 2\pi$ in their strongly stratified case where $Re_b \approx 2$, we can get $L_d \approx 0.03$, which is very close to the test-filter width in their simulation. Hence, we speculate that if their test cutoff filter k_c was decreased, their spectral backscatter would also be decreased and finally eliminated. As a result, the upscale energy transfer in wavenumber space could be due to viscous effects rather than a turbulent mechanism. These findings suggest that the upscale energy transfer reported by Remmler & Hickel [21] may be due to effects of the low Reynolds number and filtering the viscous scale.

When $Re_b \gtrsim 1$, the SGS energy transfer spectra display a plateau at intermediate wavenumbers along with a cusp around k_c when $k_c \gtrsim k_b$, consistent
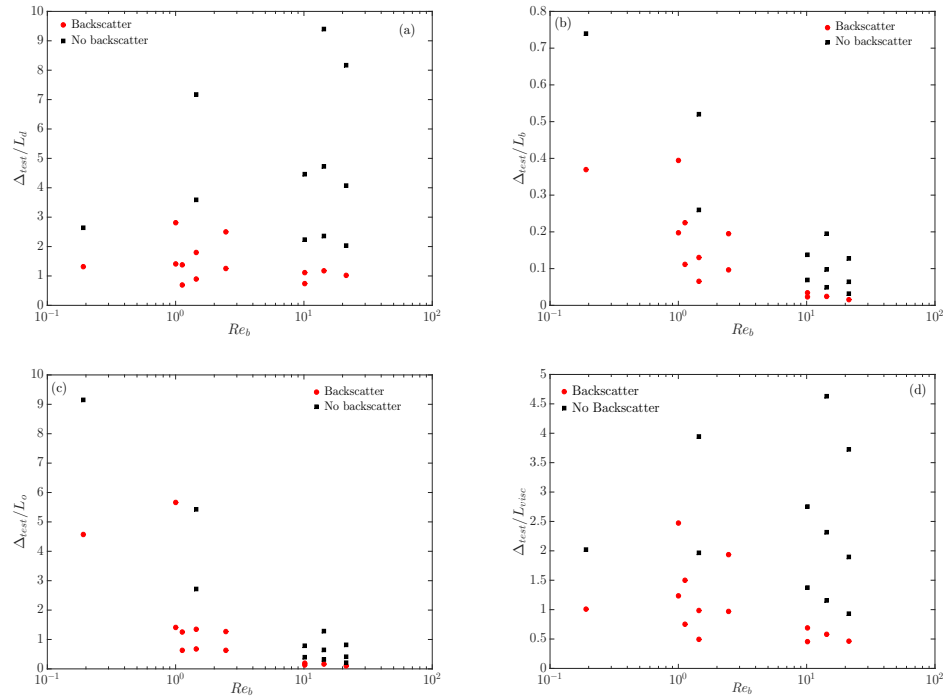
24

Figure 11: The ratios (a) Δ_{test}/L_d, (b) Δ_{test}/L_b, (c) Δ_{test}/L_o and (d) Δ_{test}/L_{visc}, versus Re_b where the red circles denote observation of spectral backscatter and the black squares show those ratios in which the spectral upscale energy transfer is eliminated; L_d, L_b, L_o, L_{visc} and Re_b are from the time of maximum ϵ.

25

with the classical picture of the Kraichnan [2] eddy viscosity and local energy transfer (figure 7). However, when $k_c < k_b$, the plateau overcomes the cusp and so the non-local SGS energy transfer becomes dominant (figure 9). In particular, for the cases with $Re_\ell = 10900$, 3030 and $Fr_\ell = 0.1$, the transfers are dominated by a cusp around k_c when $k_c = 40$ (figure 7a,b) but are dominated by non-local energy transfer at intermediate wavenumber when $k_c = 20$ (figures 9a,b), where for both cases $20 \lesssim k_b < 40$. These trends suggest that there is a non-local kinetic energy transfer from scales larger than L_b to small scales. This transfer is consistent with the evolution of the TG vortices, which are initially dominated by $k \sim 1$, into a layerwise flow with $k \sim k_b$ [19, 31]. This nonlocality in SGS energy transfer spectra might underscore the importance of resolving the buoyancy scale in LES of stratified turbulence that has been suggested in the literature [10, 22].

4.3.2. The effective turbulent Prandtl number

Figure 12 shows the averaged effective turbulent Prandtl number $\langle Pr_t(k|k_c, t) \rangle$ spectra at different test cutoffs k_c (left panels show results for $Re_b \gtrsim 1$ and right panels show those for $Re_b \lesssim 1$). The cases with $Re_\ell = 14700$, 6400 and $Fr_\ell = 0.64$, and $Re_\ell = 18000$ and $Fr_\ell = 0.48$ show positive values that are between 0 and 1, for both test cutoff $k_c = 20$ and 40 (solid purple, dashed red and green lines in figures 12a,c). However, all other cases show negative $\langle Pr_t(k|k_c, t) \rangle$ spectra over the intermediate range $0.1k_c \lesssim k \lesssim 0.6k_c$. By moving k_c from 40 to 20, negative $\langle Pr_t(k|k_c, t) \rangle$ values are decreased for cases with $Re_\ell = 3030$ and $Fr_\ell = 0.24$, 0.12 (figure 12b,d). As shown in above, the negative sign of the effective turbulent Prandtl numbers could be due to filtering the viscous scale (see figures 7, 9 and 10). It is interesting that for all cases, the averaged effective turbulent Prandtl number is positive and fairly close to 1 for k around k_c. This trend suggests that the assumption of $Pr_t \approx 1$ is reasonable for the local energy transfer at all regimes of Re_b [as is assumed in e.g. 10, 22, 32]. However, by decreasing Re_b to be of order ~ 1 or $\ll 1$, this assumption might not be valid for the nonlocal energy transfer when $\Delta_{test} \lesssim L_{visc}$.
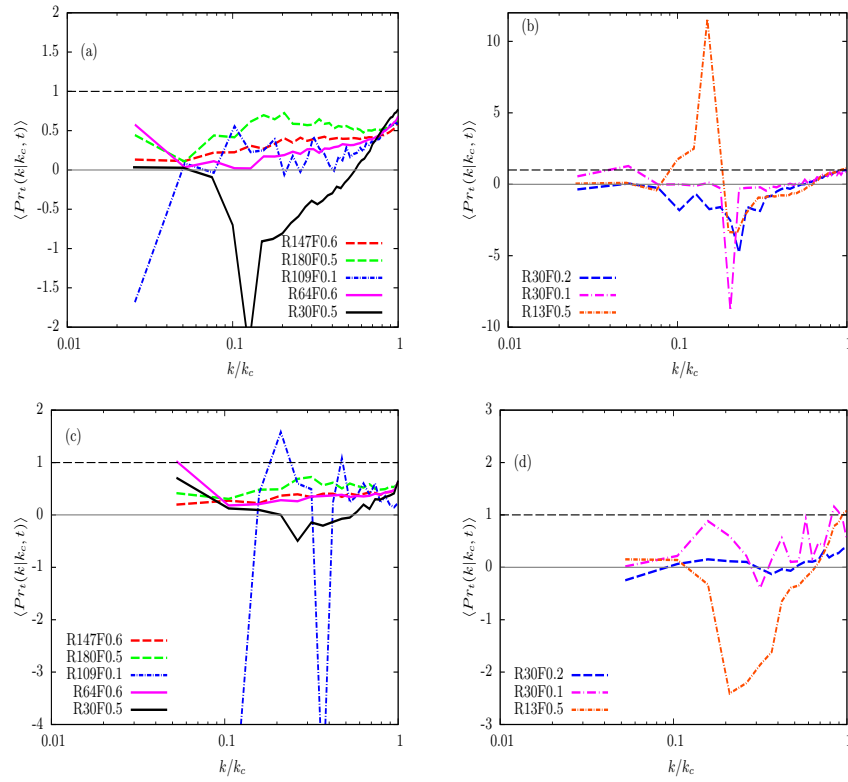
26

Figure 12: Averaged effective turbulent Prandtl number spectra for (a,b) $k_c = 40$ and (c,d) $k_c = 20$. The left panels correspond to cases with $Re_b \gtrsim 1$ and the right panels show those with $Re_b \lesssim 1$. The solid grey line and dashed black line indicate values of zero and 1, respectively.

5. Conclusion

The dynamics of kinetic and potential energy transfer around a test cutoff filter in both physical and wavenumber space for decaying stratified turbulence is studied in this paper. The effective domain-averaged SGS energy transfer ϵ_{SGS} is a small net energy transfer from large to small scales that results from the combination of two large energy transfer mechanisms: downscale ϵ^+ and upscale ϵ^- [in line with results for unstratified simulations, e.g. 4]. Increased buoyancy Reynolds number Re_b leads to an increase in the upscale and downscale kinetic and potential SGS energy transfer, and hence increasing effective SGS energy transfer in physical space. As a result, the domain-averaged upscale energy transfer might not be just a random and stochastic process that is independent of the flow dynamics, as is considered for modelling backscatter in the literature [e.g. 33, 34, 35, 36]. It is also shown that $\epsilon^\pm$ and $\varepsilon^\pm$ are not very sensitive to the location of the test cutoff k_c. Our results show that the domain-averaged backscatter depends on the parameters of stratified turbulence such as the Froude and buoyancy Reynolds numbers. A similar idea is suggested by O'Brien et al. [27], in which backscatter in reacting turbulence depends on the dynamics of the flow such as the SGS Mach number and high-speed compressibility.

In wavenumber space, the effective kinetic and potential energy transfer spectra are positive (i.e. forward scatter) when $Re_b \sim O(10)$. However, for $Re_b \sim O(1)$ or smaller, the kinetic energy transfer spectra show negative values (i.e. backscatter) when the Reynolds number is small. This behaviour occurs when the test filter scale falls below the scale of the viscous layers that are present at small Re_b, or when $\Delta_{test} \sim L_d$ even at $Re_b \gtrsim 1$. These trends suggest that the effective kinetic energy transfer spectra are contaminated by viscous effects in the small Reynolds number regime, in which backscatter are seen in the effective kinetic energy transfer spectra. In addition, our results show a non-local energy transfer from scales larger than L_b to small scales. Recently, an *a posteriori* study on LES of stratified turbulence has shown that current

28

eddy-viscosity SGS models (i.e. the Smagorinsky, dynamic Smagorinsky and Kraichnan models) require resolution of L_b to capture the fundamental features of stratified turbulence [10, 22]. DNS results of this paper suggest that the requirement of resolving L_b in LES of stratified turbulence is related to the need of resolving the non-local energy transfer around L_b, since current SGS models are developed based on the local SGS dissipation, i.e. removing energy mainly at smallest resolved scale Δ. The effective turbulent Prandtl number spectra suggest that the assumption of $Pr_t = 1$ is reasonable for the local energy transfer. For the non-local energy transfer, however, the effective $\langle Pr_t \rangle$ is negative when $Re_b \sim O(1)$ or smaller at $\Delta_{test} \sim L_d$.

Performing DNS of stratified turbulence for large and small Re_b, when the Reynolds number is very large is a potential direction for future work, so that the dynamics of energy transfer around the buoyancy and Ozmidov scales could be studied in detail, and away from the effects of molecular viscosity where L_d is very small. Also, applying different types of test filters, in particular those are common in physical space, such as the top-hat or Gaussian filters, is desirable to study the sensitivity of backscatter to the type of test filter. Moreover, it would be interesting to study spectral backscatter in simulations with large-scale potential energy forcing/initial conditions, e.g. large-scale gravity waves. In addition, an *a priori* evaluation of current SGS models in DNS of stratified turbulence will be another research avenue towards developing a new SGS model that does not require resolving L_b in LES of stratified turbulence.

6. Acknowledgement

29

[1] J. Smagorinsky, General circulation experiments with the primitive equations. I. The basic experiment *Mon. Weather Rev.* **91(3)**, 99-164 (1963).

[2] R. H. Kraichnan, Eddy viscosity in two and three dimensions. *J. Atmos. Sci.* **33**, 1521-1536 (1976).

[3] L. F. Richardson, Weather prediction by numerical process. *Cambridge University Press*, Cambridge (1922).

[4] U. Piomelli, W. H. Cabot, P. Moin, and S. Lee, Subgrid-scale backscatter in turbulent and transitional flows. *Phys. Fluids A* **3(7)**, 1766-1771 (1991).

[5] J. A. Domaradzki , W. Liu, and M. E. Brachet, An analysis of subgrid-scale interactions in numerically simulated isotropic turbulence. *Phys. Fluids A* **5**, 1747-1759 (1993).

[6] M. Germano, U. Piomelli, P. Moin, and W. H. Cabot, A dynamic subgrid-scale eddy viscosity model. *Phys. Fluids A* **3(7)**, 1760-1765 (1991).

[7] S. Ghosal, T. S. Lund, P. Moin, and K. Akselvoll, A dynamic localization model for large-eddy simulation of turbulent flows. *J. Fluid Mech.* **286**, 229-255 (1995).

[8] C. Meneveau and J. Katz, Scale-invariance and turbulence models for large-eddy simulation. *Ann. Rev. Fluid Mech.* **32**, 1-32 (2000).

[9] S. B. Pope, Turbulent Flows. *Cambridge University Press*, Cambridge (2000).

[10] S. Khani and M. L. Waite, Large eddy simulations of stratified turbulence: the dynamic Smagorinsky model. *J. Fluid Mech.* **773**, 327-344 (2015).

[11] S. Remmler and S. Hickel, Direct and large eddy simulation of stratified turbulence. *Int. J. Heat Fluid Flow* **35**, 13-24 (2012).

[12] F. Wan and F. Porté-Agel, Large-eddy simulation of stably-stratified flow over a steep hill. *Boundary-Layer Meteorol* **138**, 367-384 (2011).

[13] J. J. Riley and M.-P. Lelong, Fluid motions in the presence of strong stable stratification. *Annu. Rev. Fluid Mech.* **32**, 613-657 (2000).

[14] S. Almalkie and S. M. de Bruyn Kops, Kinetic energy dynamics in forced, homogeneous, and axisymmetric stably stratified turbulence. *J. Turbul.* **13** 1-32 (2012).

[15] P. Bartello and S. M. Tobias, Sensitivity of stratified turbulence to the buoyancy Reynolds number. *J. Fluid Mech.* **725**, 1-22 (2013).

[16] P. Billant and J.-M. Chomaz, Self-similarity of strongly stratified inviscid flows. *Phys. Fluids* **13(6)**, 1645-1651 (2001).

[17] G. Brethouwer, P. Billant, E. Lindborg, and J.-M. Chomaz, Scaling analysis and simulation of strongly stratified turbulent flows. *J. Fluid Mech.* **585**, 343-368 (2007).

[18] E. Lindborg, The energy cascade in strongly stratified fluid. *J. Fluid Mech.* **550**, 207-242 (2006).

[19] M. L. Waite and P. Bartello, Stratified turbulence dominated by vortical motion. *J. Fluid Mech.* **517**, 281-303 (2004).

[20] S. Khani and M. L. Waite, Effective eddy viscosity in stratified turbulence. *J. of Turbl.* **14(7)**, 49-70 (2013).

[21] S. Remmler and S. Hickel, Spectral eddy viscosity of stratified turbulence. *J. Fluid Mech.* **755**, R6, doi:10.1017/jfm.2014.423 (2014).

[22] S. Khani S. and M. L. Waite, Buoyancy scale effects in large-eddy simulations of stratified turbulence. *J. Fluid Mech.* **754**, 75-97 (2014).

[23] J. J. Riley and S. M. de Bruyn Kops, Dynamics of turbulence strongly influenced by buoyancy. *Phys. Fluids* **15**, 2047-2059 (2003).

[24] M. L. Waite, Stratified turbulence at the buoyancy scale. *Phys. Fluids A* **23**, 066602 (2011).

[25] C. Rorai, D. Rosenberg, A. Pouquet, and P. D. Mininni, Helicity dynamics in stratified turbulence in the absence of forcing. *Phys. Rev. E* **87**, 063007 (2013).

[26] C. Rorai, P. D. Mininni, and A. Pouquet, Turbulence comes in bursts in stably stratified flows. *Phys. Rev. E* **89**, 043002 (2014).

[27] J. O'Brien, J. Urzay, M. Ihme, P. Moin, and A. Saghafian, Subgrid-scale backscatter in reacting and inert supersonic hydrogen-air turbulent mixing layers. *J. Fluid Mech.* **743**, 554-584 (2014).

[28] R. Marino, P. D. Mininni, D. L. Rosenberg, and A. Pouquet, Large-scale anisotropy in stably stratified rotating flows. *Phys. Rev. E* **90**, 023018 (2014).

[29] R. Marino, A. Pouquet, and D. Rosenberg, Resolving the paradox of oceanic large-scale balance and small-scale mixing. *Phys. Rev. Lett.* **114**, 114504 (2015).

[30] M. L. Waite, Direct numerical simulations of laboratory-scale stratified turbulence. Modelling Atmospheric and Oceanic Flows: Insights

32

from Laboratory Experiments, (eds. T. von Larcher & P. Williams), *American Geophysical Union*, Washington, DC., 159-175 (2014).

[31] P. Billant and J.-M. Chomaz, Experimental evidence for a new instability of a vertical columnar vortex pair in a strongly stratified. *J. Fluid Mech.* **418**, 167-188 (2000).

[32] D. A. Siegel and J. A. Domaradzki, Large-eddy simulation of decaying stably stratified turbulence. *J. Phys. Oceanogr.* **24**, 2353-2386 (1994).

[33] J. R. Chasnov, Simulation of the Kolmogorov inertial subrange using an improved subgrid model. *Phys. Fluids A* **3(1)**, 188-200 (1991).

[34] M. Lesieur, Turbulence in Fluids. *Kluwer Acad. Publrs.* Dordrecht (1990).

[35] L. Marstorp, G. Brethouwer, and A. V. Johansson, A stochastic subgrid model with application to turbulent flow and scalar mixing. *Phys. Fluids* **19**, 035107 (2007).

[36] S. Weinbrecht and P. J. Mason Stochastic backscatter for cloud-resolving models. Part I: implementation and testing in a dry convective boundary layer. *J. Atmos. Sci.* **65**, 123-139 (2008).